MATEC Web of Conferences **366**, 01002 (2022) https://doi.org/10.1051/matecconf/202236601002
Power Transmissions 2022

Factors influencing actuator's backdrivability in human-centered robotics

Pablo Lopez Garcia[1,2,*], *Elias* Saerens[1], *Stein* Crispel[1,2], *Anand* Varadharajan[1,2], *Dirk* Lefeber[1,2], and *Tom* Verstraten[1,2]

[1]VRIJE UNIVERSITEIT BRUSSEL, 1050 Brussels, Belgium
[2]FLANDERS MAKE, 3001 Leuven, Belgium

Abstract. Human-Centered Robotics aims to use robotic devices to improve our life. In Europe alone, around 650.000 people live with limb amputations, 40 Mio. have jobs with high of lumbar injuries, and 40 Mio. are 80+ years. Worldwide, active prostheses, exoskeletons, and service robots could help improve these people's lives. However, their adoption is unfortunately strongly hindered by technological limitations in the actuators powering these devices.

Backdrivability characterizes an actuator's ability to be driven from the load side, and it is a crucial property to enabling capable human-centered robotic devices. In this paper, we describe the underlying factors that determine actuator backdrivability in robotics and investigate suitable scaling laws to understand how these factors are conditioned by the motor and gearbox selection and the specific operational cycle of a robotic device. This analysis unveils the complexity and challenges faced to accurately model and predict this complex phenomenon, contradicting an extended hypothesis in the robotics community that sees low-ratio transmissions as the best strategy to build backdrivable, lightweight actuators.

1 Introduction

Data collected from *statista.com* indicates that, in Europe alone, around 650.000 people live with limb amputations, 40 Mio. have jobs with high risk of lumbar injuries, and 40 Mio. are 80+ years. Human-centered robotic devices – active prostheses, exoskeletons, service robots,… – could improve the lives of these people, but this potential is currently hindered by some technological limitations of the actuators used to power these devices.

Backdrivability characterizes the ability of an actuator to operate in reverse direction (driven from its output), enabling power flow from the outside world (load) into the motor. In [1], this meaning is restricted to breakaway conditions (starting the movement). Here, we follow the example of Nef. et al. [2] to extend backdrivability beyond breakaway conditions to include other operating conditions relevant for bidirectional energy exchange.

In conventional industrial robots, robustness is linked to robot's ability not to deviate from its position trajectory (dX) under an external disturbance force (dF). In contrast, in human-centered robotics, the close interaction between robots and humans requires low forces (dF) when there is a deviation from the position trajectory (dX) [3]. This makes operator safety a crucial constraint and links it to low mechanical impedance (dX/dF) – backdrivability – during interaction [4]. Accordingly, backdrivability can render human-robot collaboration safer, canceling the need for exteroceptive torque sensors and enabling broader control bandwidths [5].

The narrow link between backdrivability and control is also highlighted in haptics and fast-legged locomotion. In [6], the authors emphasize the importance of transmission transparency – closely related to actuator's backdrivability – to achieve good control performance in haptic devices and to cope with high forces and accelerations in fast-legged locomotion. When high contact forces are involved, good backdrivability helps also preserve the actuator's integrity. Comparing to biological muscles, Seok et al. assign pivotal relevance to the trade-off between torque density and backdrivability in electromagnetic actuation [6].

Beyond its crucial impact on safety and control, specific robotic applications may have other backdrivability requirements. In rehabilitation, backdrivability allows assist-as-needed control strategies that encourage patients' participation and movement capability assessment [2]. In devices manually programmed by demonstration, such as cobots, backdrivability allows this operation with unpowered actuators, simplifying and reducing energy consumption [7]. On the other hand, in prosthetics and cobots, limited backdrivability can help hold a static position under load when the actuators are unpowered, enabling significant efficiency gains [5] and the use of lighter brakes.

This paper's contribution lies in providing a holistic review of how design decisions on robotic actuation condition backdrivability and thus robotic performance. In the next section, we use the concept of reflected mechanical impedance to model the backdrivability of an

* Corresponding author: plopezga@vub.be

actuator and describe its main components. Section 3 compiles the scaling laws to link these components with essential design choices for robotic actuation. Finally, the influence on overall actuator's backdrivability of the operating cycle is established through their differentiated effect on the main backdrivability parameters. A conclusion section closes this analysis.

2 Reflected Mechanical Impedance

We consider a conventional, reference robotic actuator consisting of an electric motor and a compact gearbox, as shown in Fig. 1.

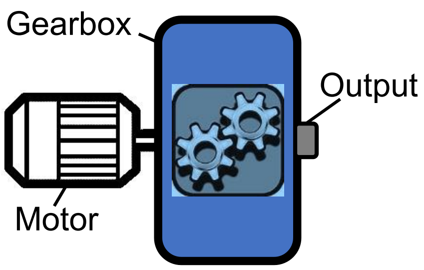

Fig. 1. Conventional, reference robotic actuator consisting of an electric motor and some form of a compact gearbox.

The backdrivability of such an actuator is characterized by the *mechanical impedance* seen from its output (the *load* side). It corresponds to the frequency-dependent relationship between resistive joint torques and angles [8] when driving the actuator from its natural output. Our proposed model sees the actuator as a mass-spring-damper system with added Coulomb friction, such that we can describe the mechanical impedance of an actuator's output through the equation of motion:

$$\tau_{bck} = J_{bck} \cdot \ddot{\theta_O} + D_{bck} \cdot \dot{\theta_O} + K_{bck} \cdot \theta_O + \tau_C + \tau_m \qquad (1)$$

τ_{bck} : backdriving torque

J_{bck} : backdriving moment of inertia along the rotor axis

D_{bck} : backdriving damping coefficient

K_{bck} : backdriving stiffness

θ_O : angular displacement of the actuator's output

τ_C : Coulomb (speed-independent) friction

τ_m : Torque supplied by the motor

2.1 Backdriving Inertia

Inertia characterizes the resistance of matter to any change in a body's momentum (product of mass and velocity). The speed-reduction ratio has a substantial impact on inertia. If we fix a body with inertia J_m to the input of a gearbox, like, for example, the rotor of a motor in Fig. 1, and we then subject the gearbox to a backdriving torque τ_b, the body inertia is perceived from the gearbox output as a backdriving inertia J_b given by:

$$J_{bck} = \frac{\tau_{bck}}{\ddot{\theta}_O} = \frac{i_g \cdot \tau_I}{\left(\frac{\ddot{\theta}_I}{i_g}\right) \cdot \eta'_0} = \frac{i_g^2 \cdot J_I}{\eta_0} \qquad (2)$$

η'_0 : gearbox's backdriving efficiency under τ_{bck}

i_g : gearbox's reduction ratio

τ_I : torque seen at the gearbox input under τ_b

θ_I : angular displacement on gearbox input under τ_b

Fig. 2 shows a simple inertia model of a robotic actuator, corresponding to the description of Fig.1, in which the effect of efficiency is not included for simplicity. To account for the different angular speeds in the actuator, we assume a planetary configuration as a reference, in which the different elements are grouped based on same angular speed (and thus the same angular acceleration). The speed-reduction ratios are highlighted as orange boxes between the different gearbox elements.

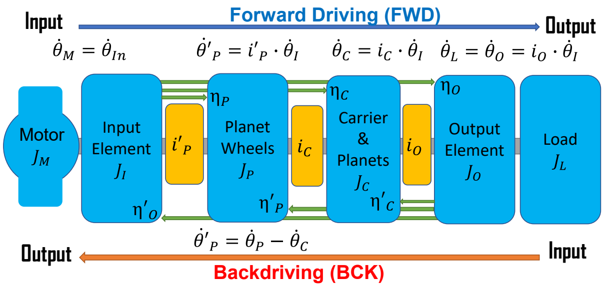

Fig. 2. Inertia model of a conventional robotic actuator from Fig.1. The compact robotic gearbox includes an input element, a carrier, one or more planet wheels, and an output element. Two operation modes are shown: (i) forward driving, with the motor driving the system and the load, and (ii) backdriving, when a backdriving load torque drives the actuator (and thus the motor). The actuator's constitutive elements are shown as blue boxes, while speed-reduction ratios relative to the gearbox input i'_P, i_C, i_O are shown as orange boxes.

From left to right (forward driving direction), we first encounter the inertia of the electric motor's movable parts (rotor), fixed to the input element of the gearbox, which rotate at the same speed and around the same motor axis. Then, a first speed reduction ratio i'_P is encountered to account for a lower rotation speed of the planet-wheels around their own axis. The same procedure is used for the carrier subassembly element, which in this case rotates around the gearbox axis and includes the inertia of the planet wheels to this specific movement. Then again for the output element of the gearbox, which rotates at the same speed as the load, again around the gearbox central axis. This allows writing the forward-driving system inertia as:

$$J_{fwd} = (J_M + J_I) + \frac{J_{P1}}{\eta_P \cdot i'^2_P} + \frac{J_C}{\eta_C \cdot i_C^2} + \frac{(J_L + J_O)}{\eta_O \cdot i_O^2} \qquad (3)$$

where *J* respectively represents the inertia of the elements motor *(M)*, input *(I)*, planet-wheels *(P)*, carrier and planet-wheels *(C)*, output *(O)*, and load *(L)*, shown in Fig.2, and η_x is an efficiency that takes into account the torque losses incurred from the gearbox input until the element "x," which represents either the planet-wheels (*x=P*), carrier, and planet-wheels (*x=C*), or the gearbox output (*x=O*).

From right to left (now thus in backdriving direction), we can do an analogous exercise to establish the backdriving's inertia of the system as:

$$J_{bck} = i_O^2 \cdot \frac{(J_M+J_I)}{\eta'_O} + \frac{i_O^2 \cdot}{i'^2_P} \cdot \frac{J_P}{\eta'_P} + \frac{i_O^2 \cdot}{i_C^2} \cdot \frac{J_C}{\eta'_C} + (J_L + J_O) \quad (4)$$

where η'_x represents now an efficiency that takes into account the torque losses incurred from the gearbox output until the same element "x" as in (3).

In this exercise, the compound movement of the planet wheels – simultaneously rotating around their own axis and around the central axis of the gearbox – requires including the two corresponding inertias in our equations. For the rotation around its own axis, the right angular speed is $\dot{\theta}'_P$, seen from a non-inertial frame fixed to the carrier element and given by:

$$\dot{\theta}'_P = \dot{\theta}_P - \dot{\theta}_C = i'_P \cdot \dot{\theta}_I \quad (5)$$

Comparing equations (3) and (4) and assuming in first instance that the forward and backdriving gearbox efficiencies are high enough to be disregarded ($\eta_x \approx \eta'_x \approx 1$ for x = O, P, C), we can write:

$$J_{bck} \approx i_O^2 \cdot J_{fwd} \quad (6)$$

This indicates that, even when the actuator includes a gearbox with multiple stages, the backdriving inertia of the actuator is approximately equal to its forward inertia multiplied by the square of the reduction ratio of the gearbox in the actuator. As previously indicated, the accuracy of this approximation is directly dependent on the efficiency of the gearbox.

Equations (3) and (4) highlight the high relevance of the speed reduction ratios in a gearbox's inertia. When high ratios are involved, equation (3) shows that during forward driving, most of the actuator's inertia that must be accelerated is usually that of the motor's rotor and the gearbox's input element. The effective inertia of the other gearbox's elements and the load are substantially reduced by the effect of the squared reduction ratios.

Similarly, when large speed-reduction ratios are involved, equation (4) indicates that the inertias of the motor's rotor and the gearbox's input could play a dominant role in the backdriving inertia of the actuator, owing again to the effect of the squared gearbox reduction ratios. In [9], a numerical example with real data is provided, confirming that using only rotor inertia and gearbox input inertia to calculate actuator's inertia is, in this case, a good approximation.

Yet, it is important to put in perspective the validity of this approach: inertia can also scale very fast with size, particularly in radial direction. In actuators where only moderate reduction ratios are used either for the complete gearbox or internally, between its constitutive elements, or which have substantial size differences in radial direction between stages, this approximation does not hold. In these cases, it is necessary to analyze the inertias and speeds of the different gearbox components separately and eventually also of the load. Indeed, suppose we calculate the moment of inertia for a cylinder (shaft), which is a valid first approximation for many of the rotating parts in a gearbox and an electric motor. In that case, we can see that inertia increases with the 4th power of the shaft's diameter:

$$J_{shaft} = \frac{1}{2} \cdot M \cdot r_{shaft}^2 = \frac{\pi}{2} \cdot \rho \cdot L \cdot r_{shaft}^4 \quad (7)$$

J_{shaft} : moment of inertia of a shaft

M : mass of the shaft

r_{shaft} : radius of the shaft

ρ : density of the material

L : length of the shaft

2.2 Backdriving Losses

Friction influences the backdriving torque through two main components, according to equation (1): backdriving damping and Coulomb friction. Additionally, resistive Joule losses must also be included for the motor:

$$\tau_L = \tau_C + \tau_D + \tau_R \quad (8)$$

τ_L : actuator's total loss torque, seen from its output

τ_C : actuator's Coulomb friction torque

τ_D : actuator's viscous friction torque

τ_D : actuator's resistive (Joule) losses torque

2.2.1 Gearbox Losses

Gearbox losses can be classified depending on the element in which they originated, differentiating into load-dependent and load-independent losses, assuming that these two are independent of each other [10]:

$$P_{L,g} = P_{LZ} + P_{LZ0} + P_{LB} + P_{LB0} + P_{LD} + P_{LX} \quad (9)$$

$P_{L,g}$: total power losses

P_{Lz} : load-dependent power losses in the meshing

P_{LZ0} : no-load power losses in the meshing

P_{LB} : load-dependent power losses in the bearing

P_{LB0} : no-load power losses in the bearing

P_{LD} : power losses in the sealings

P_{LX} : other power losses

Load-dependent losses (particularly those in the meshing) tend to be dominant at high loads [11] and explain why some backdrivability studies [12] consider only these. Yet, in our experience, the conditions required to initiate the movement – ideally with moderate output torques – are particularly important in characterizing backdrivability. Thus, it is essential to incorporate a no-load losses component capable of representing the breakaway friction – based on the Stribeck model [2] – to the total viscous and Coulomb losses from equation (1). From (5), we define:

$$\tau_{C,g} = \tau_{CZ,g} + \tau_{C0,g} = \mu_g \cdot \tau_{bck} + \tau_{C0,g} \quad (10)$$

$$\tau_{D,g} = D_{gS} \cdot e^{-\beta_g \cdot \dot{\theta}_o} + D_{gD} \cdot \dot{\theta}_O \quad (11)$$

$\tau_{C,g}$: gearbox's Coulomb friction torque

$\tau_{CZ,g}$: gearbox's load-dependent Coulomb friction torque

$\tau_{C0,g}$: gearbox's load-independent Coulomb friction torque

μ_g : gearbox's Coulomb-friction coefficient

$\tau_{D,g}$: gearbox's viscous friction torque

D_{gS} : static friction factor, dominant at near-zero speeds

D_{gD} : dynamic friction factor, dominant at higher speeds

β_g : gearbox's lubrication transition coefficient

2.2.2 Motor Losses

Losses in electrical DC motors are also very different in nature and can be split into Joule (resistive) losses in the windings, Brush-drop losses (brushed DC motors), Mechanical friction losses, Core losses due to the rotating magnets, and Stray-load losses that account for extra losses occurring at high loads [13]:

$$P_{L,m} \approx P_{RJ} + P_{BR} + P_{ME} + P_{CO} + P_{ST} \quad (12)$$

$P_{L,m}$: motor losses

P_{RJ} : resistive (Joule) losses in the motor windings

P_{BR} : brush-drop losses

P_{ME} : mechanical friction losses

P_{CO} : core losses

P_{ST} : stray-load losses

Joule losses originate due to the motor winding resistance causing a voltage drop proportional to the current I delivered by the motor. This leads to a dissipation of power which amounts to $P_{RJ} = R \cdot I^2$, where R stands for the total winding resistance. In robotics, this is often the main source of power loss [14]. Joule losses are also known under several different names, such as "resistive losses", "copper losses", "Ohmic losses" or "heating losses".

Brush-drop losses: Brushed DC motors rely on graphite brushes to transfer current from the stator to the rotor. The current transfer results in a power loss of

$$P_{BR} = I \cdot \Delta V_{brush} \quad (13)$$

where ΔV_{brush} is the voltage drop across the brushes. The voltage drop depends on the composition of the brushes, contact pressure and the condition of the surface of the commutator, and must therefore be determined for every machine. Nevertheless, it is often assumed to be constant, with a value of $\Delta V_{brush} = 2V$ [15]. The brush-drop losses are therefore often approximated as $P_{BR} \approx 2 \cdot I$, i.e., proportional to the current.

Mechanical (friction) losses are mostly due to friction in the bearings, aerodynamic drag experienced by the rotor and often called windage losses, and – in the case of brushed DC motor – friction between the brushes and the commutator. These losses can be considered proportional to motor speed $\dot{\theta}_m$ (Coulomb friction) and, to some extent, to $\dot{\theta}_m^2$ (viscous friction). Windage losses are typically considered to be proportional to $\dot{\theta}_m^3$ [15]. In some cases, static mechanical friction losses can also be relevant.

Core losses are linked to the rotating magnetic field. They can be subdivided into two main contributions. Hysteresis (re-magnetization or magnetic losses) losses represent the hysteresis in the motor curve, which is caused by the fact that some energy is needed to reverse the direction of the magnetic field, leading to a power loss $P_{remag} = \tau_{magn} \cdot \dot{\theta}_m$, with τ_{magn} the torque needed for reversal of magnetization. Hysteresis losses are thus proportional to speed, similar to Coulomb friction. Secondly, there will be losses due to eddy currents in the magnetic core (iron losses). Eddy current losses are proportional to $\dot{\theta}_m^2$ and, can thus mathematically be included in the viscous friction losses.

Stray losses account for extra losses occurring at high loads. They are mainly related to pulsations in the flux, caused primarily by the short-circuit current in the coil undergoing commutation. Stray losses are only relevant for large-size machines and can be neglected for small-size motors [14].

This classification allows us to write:

$$\tau_{F,m} = \tau_{R,m} + \tau_{C0,m} + \tau_{D,m} + \tau_{W,m} + \tau_{BR,m} \approx \quad (14)$$

$$\approx R \frac{\tau_{bck}^2}{i_O^2 {\eta'}_O^2 k_t^2} \frac{1}{\dot{\theta}_O} + i_O \tau_{C0,m} + i_O D_{mS} e^{-\beta_m \cdot i_O \dot{\theta}_o} + i_O^2 D_{mD} \dot{\theta}_O \quad (15)$$

assuming small EC motors without brushes and negligible windage losses, as typically used in the robotics field.

R : winding resistance

τ_m : torque delivered by the motor

k_t : torque constant of the motor

$\tau_{L,m}$: motor's total loss torque

$\tau_{R,m}$: motor's resistance friction torque

$\tau_{C0,m}$: motor's Coulomb loss torque, load-independent

$\tau_{D,m}$: motor's viscous losses torque

$\tau_{W,m}$: motor's windage losses torque

$\tau_{BR,m}$: motor's brush-drop losses torque

${\eta'}_0$: gearbox's backdriving efficiency

D_{mS} : static friction factor, dominant at near-zero speeds

D_{mD} : dynamic friction factor, dominant at higher speeds

β_m : motor's lubrication transition coefficient

2.2.3 Discussion on Backdriving Losses

According to our model, robotic gearbox and motor losses can be classified according to the chart in Fig. 3.

The influence of the speed-reduction ratio is not explicitly highlighted through the approach we have used to model losses during backdriving. Yet, it is worth reflecting on how it affects the relative impact of the different friction contributions, which in this case is less trivial than inertia. Dynamic viscous friction is naturally strongly dependent on speed, such that these losses tend to become relevant only after the movement is initiated.

Consequently, the larger dynamic viscous losses in an actuator are typically encountered on the high-speed side, that is, the motor (D_{mD}) and the input elements of the gearbox (D_{gD}).

A similar reflection can also be done about the motor's resistive electrical losses. Motor torques (and thus currents through the windings) are usually moderate during backdriving, so resistive backdriving losses can generally be disregarded. When braking regeneration techniques are used, backdriving motor torques and resistive losses tend to be more significant. In this case, a considerable part of the electrical losses could be generated in the motor driver's power stage and incorporating those into the model should be evaluated.

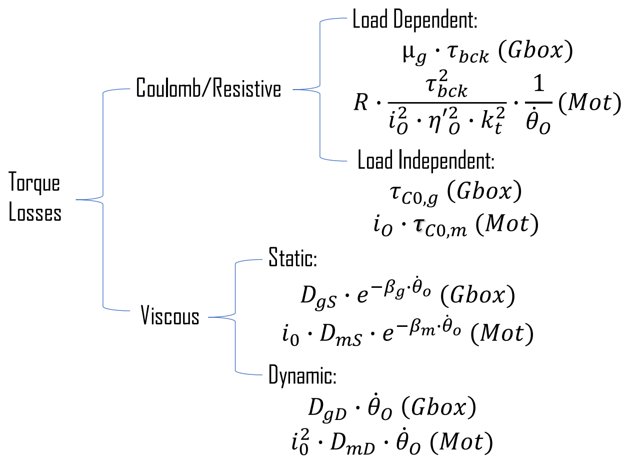

Fig. 3. Classification of the Torque Losses in the gearbox (Gbox) and electric motor (Mot) of an electric actuator

2.3 Backdriving Stiffness

Mechanical stiffness is the derivative of torque with respect to angular position. The gearbox speed-reduction ratio has again a substantial impact on how the torsional stiffness K_I of a spring fixed to its input is perceived from the output as a backdriving stiffness K_{bck}:

$$K_{bck} = \frac{d(\tau_{bck}^*)}{d\theta_O^*} = \frac{i_g \cdot \eta_g \cdot \tau_I}{\left(\frac{\theta_I}{i_g}\right)} = \eta_{g,s} \cdot i_g^2 \cdot K_I \qquad (16)$$

τ_{bck}^* : output torque applied on a fixed spring end

θ_O^* : angular displacement on gearbox output under τ_{bck}^*

Comparing this equation with (2), we see that speed-reduction ratios have an analogous impact on backdriving stiffness and inertia. Yet, there is a fundamental difference in how these two properties accumulate for devices connected in series. For inertia, the equivalent inertia of two elements connected in series is the sum of the two inertias. For Stiffness, their equivalent stiffness does not correspond to the direct sum of the two stiffnesses but to their product divided by their sum. In order to obtain a similar equation as in (4), we can use instead the mechanical compliance (C, inverse of stiffness), which has the advantage that it can be directly added for elements connected in series:

$$C_b = \frac{1}{K_b} = \frac{\theta_O^*}{\tau_b^*} = \frac{\left(\frac{\theta_I}{i_g}\right)}{i_g \cdot \eta_g \cdot \tau_I} = \frac{C_I}{\eta_{g,s} \cdot i_g^2}; \qquad (17)$$

C_b : backdriving compliance

C_I : torsional compliance of a spring on the gearbox input

When higher reduction ratios are involved, equation (17) indicates that the compliance of the input elements will be substantially reduced by a factor close to the square of the speed-reduction ratio when reflected to the gearbox's output, thus making them practically negligible for the overall compliance (stiffness) of the system. Yet, rotational compliance is proportional to the inverse of the polar moment of inertia, which for shaft-like, cylindrical bodies, increases again with the 4th exponent of the radius, as it was the case for inertia as we saw in equation (7):

$$K_{shaft} = \frac{\pi}{2} \cdot r_{shaft}^4 \cdot \left(\frac{G}{L}\right) \qquad (18)$$

K_{shaft} : torsional compliance of a cylindrical shaft

r_{shaft} : radius of the shaft

G : modulus of rigidity of the shaft's material

L : length of the shaft

This indicates again that changes in size, particularly in radial direction, can rapidly become more relevant than the effect of the speed-reduction ratios, particularly if the speed-reduction ratios are moderate.

The equation describing the overall system behavior, written in terms of compliance for convenience, becomes:

$$C_{bck} = \frac{\eta'_O (C_M + C_I)}{i_O^2} + \frac{\eta'_P i'^2_P C_P}{i_O^2} + \frac{\eta'_C i_P^2 C_C}{i_O^2} + (C_L + C_O) \quad (19)$$

3 Scaling Laws

Scaling laws are practical tools used in engineering to predict the impact of a reduced set of significant variables on another system variable of interest. Often, these relationships are complex in nature and involve substantial interdependencies with other variables and design parameters. In scaling laws, accurate observation of these interdependencies is typically sacrificed to obtain a generic rule that provides an approximate yet intuitive idea of the underlying relationship between the significant variables and the system variable.

In this sense, the following subsections explore to which extent practical scaling laws can be developed to intuitively understand how the backdriving parameters of an actuator's gearbox and motor are related to its geometry, speed-reduction ratio, and torque capability.

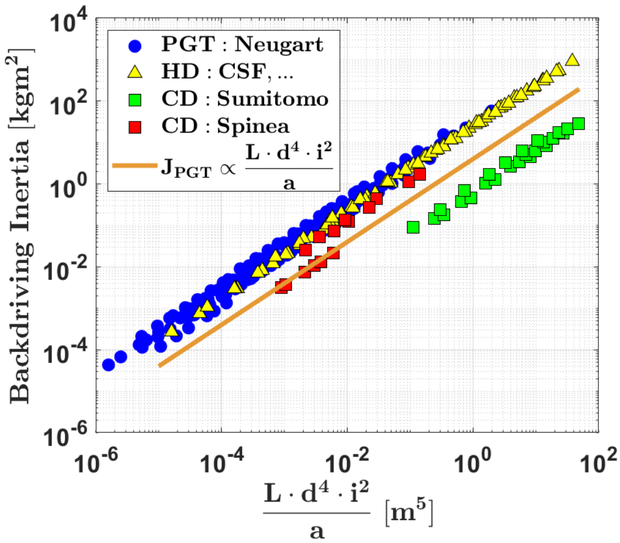

Fig. 4. Correlation of the proposed geometric scaling laws of backdriving inertia of equation (21) with planetary (PGT) transmissions from Neugart, Harmonic Drives (HD) of the CSF, CSG, SHF, SHG, and HFUS series, and Cycloid Drives (CD) of the Sumitomo FC T-series, data from [16], and the Spinea CD G- series. The curves (PGT, HD, CD) follow a linear trend reasonably parallel to that of the proposed law, which in logarithmic representation indicates that the backdriving inertia is a lineal function of the proposed law. The backdriving inertia is calculated from the input inertia given in the catalogue, multiplied by the square of the speed-reduction ratio, thus disregarding the effects of the gearbox's internal efficiency. Note that the backdriving inertias of the HD and PGT are comparable, while the inertias of the CD are substantially lower for Sumitomo. For Spinea, which was not included in the study in [16], the G- series seems to have two differentiated constructive solutions with an offset with respect to each other.

3.1 Scaling backdriving Inertia

To establish the scaling laws linking backdriving inertia with torque capacity and speed-reduction ratio, we can take advantage of the dimensional scaling laws set in our previous work for some of these parameters.

3.1.1 Gearbox inertia scaling

In [16], we demonstrated the validity of the following scaling laws, derived analytically, and validated empirically for different types of robotic transmissions:

(a) For conventional planetary gearboxes (PGT):

$$J_{PGT} \propto \left(\frac{L_g \cdot d_g^4 \cdot i_g^2}{a}\right) \tag{20}$$

L_g : axial length of the gearbox

d_g : outer diameter of the gearbox

a : number of planetary stages of the gearbox

(b) For Harmonic Drive (HD) and Cycloid Drive (CD) transmissions:

$$J_{HD} \propto \left(L_g \cdot d_g^4 \cdot i_g^2\right) \propto J_{CD} \tag{21}$$

These laws provide an accurate tool for predicting how geometry and speed-reduction ratio will affect inertia, as we can see graphically in Fig.4.

3.1.2 Motor inertia scaling

The following scaling law for the rotor's inertia of an electric motor is generally adopted [17], [6], [18]:

$$J_m \propto \left(L_m \cdot r_{gap}^3\right) \propto \left(L_m \cdot d_m^3\right) \tag{22}$$

L_m : axial length of the motor

r_{gap} : radius of the magnetic interface rotor-stator

d_m : outer diameter of the motor

Yet, our analysis using Maxon EC and EC-Flat motors frequently used in the robotic community indicates that the following empirical scaling law is actually closer to the observed behavior, as shown in Fig. 5:

$$J_m \propto \left(L_m \cdot d_m^4\right) \tag{23}$$

This equation also seems reasonable from an analytic point of view. If we assume that the mass of the motor is approximately proportional to the product of its length and section area, its moment of inertia is roughly proportional to the mass multiplied by the square of its diameter, as is the case for a solid cylinder.

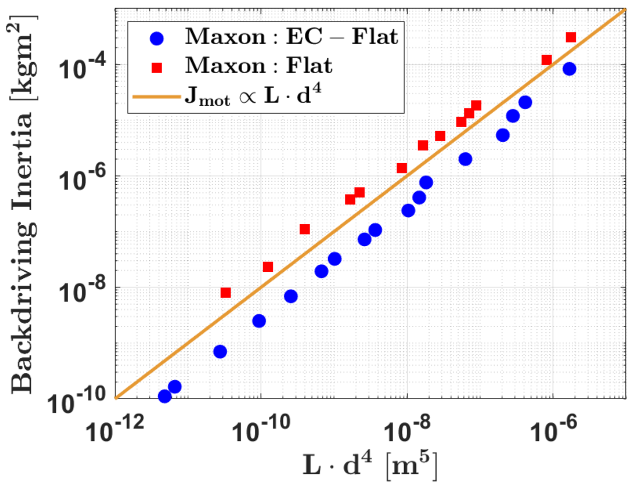

Figure 5. Correlation of the proposed geometric scaling law from equation (23) with rotor inertia in Maxon electric motors from EC and Flat series, data from [16].

3.2 Scaling Backdriving Losses

As we saw in 2.2, the nature of backdriving gearbox and motor losses is quite complex. Consequently, we have not succeeded in determining simple analytic scaling laws that can describe with reasonable accuracy how these losses are related to the torque and speed-reduction ratio of a gearbox or an electric motor.

Additionally, manufacturers of gearboxes and motors generally do not provide sufficient data to characterize their losses accurately, according to our model in Fig. 3. In order to obtain an intuitive idea of how design choices affect losses in these devices, we have tried a more practical approach, focusing our analysis on the data available from their datasheets and exploring these data to identify suitable scaling laws for their losses.

3.2.1 Gearbox losses scaling

PGT manufacturers typically include only the efficiency at full load in their datasheet. CD and HD manufacturers include additionally the maximum torque required to backdrive the gearbox and graphs to characterize the efficiency's dependency on input speed, output load, and temperature.

The backdriving torque is a useful tool to predict backdrivability during breakaway, while the efficiency graphs allow determining the levels of Coulomb and dynamic viscous friction during regenerative backdriving.

3.2.2 Motor losses scaling

Motor manufacturers conventionally assume that electrical losses (Joule losses in the winding) are largely dominant and do not include elements in their datasheets to describe in detail mechanical losses. The dynamic part of a motor's viscous damping torque can be estimated using the no-load current $I_{m,nl}$ and the no-load angular velocity $\dot{\theta}_{m,nl}$ [19]:

$$D_{mD} \approx \frac{k_t \cdot I_{m,nl}}{\dot{\theta}_{m,nl}} \qquad (24)$$

Other mechanical losses, including static viscous friction and Coulomb friction, are generally disregarded [19]. Although this is an effective strategy for normal motor operation, where the electrical losses tend to be largely dominant, its validity during regenerative operation is not yet confirmed. Specifically, static viscous losses and load-independent Coulomb friction can have a substantial relevance during breakaway backdriving that recommend a specific experimental characterization of these losses if a more detailed model is needed.

3.3 Scaling Backdriving Stiffness

The torsional stiffness of a given body is again strongly related to its geometry, as it was the case for inertia. This provides a possibility to attempt the derivation of analytic scaling laws. Equation (18) relates the torsional compliance (inverse of stiffness) of a solid cylinder and, assuming the same material – and thus same modulus of rigidity – announces a potentially relevant scaling rule given by:

$$K_{shaft} \propto (L \cdot d_{sh}^4) \qquad (25)$$

3.3.1 Gearbox stiffness scaling

Fig. 6 shows that the slope of the trend for Spinea CDs and Neugart PGTs provides a reasonable match with the predictions of equation (24). For PGTs, there is also a clearly identifiable effect of the number of stages not included in this equation: Neugart's catalog shows that, for a PGT, a larger number of stages results in a longer gearbox that does not increase stiffness proportionally, as predicted by equation (24). This phenomenon is behind the four series (one per gearbox diameter) of three points (for one, two, and three stages) that the Alpha gearbox series of Neugart shows in Fig. 6. In addition, a notable deviation is also recognizable for the largest size of the Neugart models analyzed, which shows a lower torsional stiffness than the trend and imposes an additional validity limitation for the scaling rule given by equation (25).

For HD, Fig. 6 shows also that this scaling law does not provide an accurate prediction. In this case, a closer analysis shows that this deviation is related to the effect of the speed-reduction ratio, not covered by equation (25): HD gearboxes show a considerable gain in torsional stiffness with higher speed-reduction ratios, which is not present in CD and PGT gearboxes and tends to saturate as the speed-reduction ratio increases. Beyond 80:1, a further increase does not lead to higher stiffness.

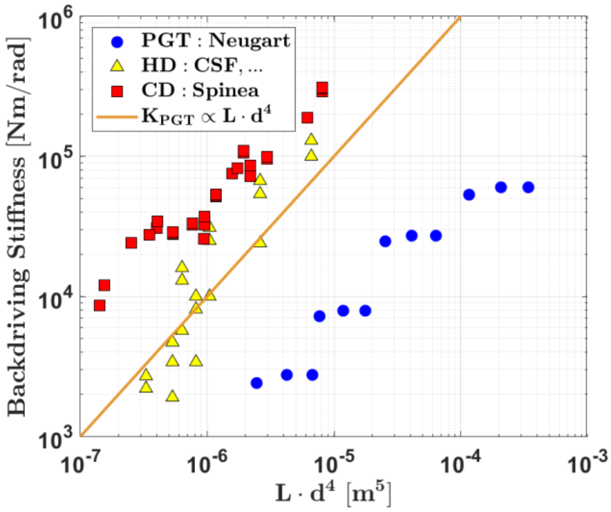

Figure 6. Correlation of the proposed geometric scaling laws for gearbox stiffness given by equation (24) using catalog data from Neugart (Alpha series), Harmonic Drive (CSF, CSG, SHF, SHG, HFUS series), and Spinea cycloid drives (G, T, E, H, and M series). The correlation provides a reasonable trend match for Spinea but shows significant limitations for Neugart and HD.

Gearbox manufacturers directly include the backdriving stiffness in their datasheet such that it is unnecessary to correct these values with the speed-reduction ratio, as we had to do for inertia calculations.

3.3.2 Motor stiffness scaling

For motors, stiffness is not a parameter systematically included by the manufacturers in datasheets. This renders it not possible for us to verify the validity of equation (25) for motors. In addition, a closer look at how electrical motors is designed indicates that other non-geometrical parameters may actually play a considerable role.

Our experience indicates that the motor's output shaft could have a fundamental contribution to its backdriving stiffness. Practically, the dimension of the motor's output shaft is chosen to provide sufficient torsional rigidity to withstand the maximum output torque of the motor, with a certain safety coefficient. Accordingly, motor torque could provide a scaling law for motor stiffness. Yet, there is unfortunately also a limitation to this approach: manufacturers use different windings on a given motor configuration to adapt the motor to different applications. Although this substantially affects the motor's output torque, the shaft diameter is not typically adjusted, as this would lead to complex and expensive modifications. This means that our torque scaling rule can only be valid if we include in our analysis only the motor configurations with the highest torque. Again, as motor stiffness is typically not specified by manufacturers, it is unfortunately not possible for us at this stage to validate any of these approaches until a broad empirical study is available.

3.4 Scaling Torque Capacity

3.4.1 Gearbox torque scaling

The following torque scaling laws are developed in [16] for different types of robotic transmissions:

(a) For conventional planetary gearboxes (PGT):

$$\tau_{PGT} \propto \left(\frac{L_g \cdot d_g^2}{a}\right) \tag{26}$$

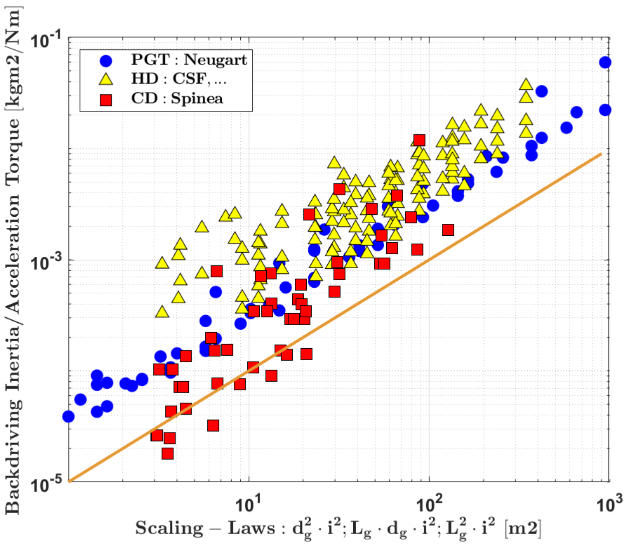

Fig. 7. Correlation between backdriving inertia and acceleration (maximum repeatable) torque capacity for Planetary Gearboxes Neugart (Alpha series), Harmonic Drive (CSF, CSG, SHF, SHG, HFUS series), and Spinea cycloid drives (G, T, E, H, and M series). The trend matches acceptably well with equation (26) for the PGTs, but it is not accurate for HD – equation (30) – and CD – equation (33) – gearboxes.

This allows us to relate torque capacity, backdriving inertia, and stiffness with the following scaling laws:

$$\frac{J_{PGT}}{\tau_{PGT}} \propto \left(d_g^2 \cdot i_g^2\right) \tag{27}$$

$$\frac{K_{PGT}}{\tau_{PGT}} \propto d_g^2 \tag{28}$$

(b) For Harmonic Drive (HD) transmissions:

$$\tau_{HD} \propto \left(d_g^3\right) \tag{29}$$

$$\frac{J_{HD}}{\tau_{HD}} \propto \left(L_g \cdot d_g \cdot i_g^2\right) \tag{30}$$

$$\frac{K_{HD}}{\tau_{HD}} \propto L_g \cdot d_g \tag{31}$$

(c) For Cycloid Drive (CD) transmissions:

$$\tau_{CD} \propto \left(\frac{d_g^4}{L_g}\right) \tag{32}$$

$$\frac{J_{CD}}{\tau_{CD}} \propto \left(L_g^2 \cdot i_g^2\right) \tag{33}$$

$$\frac{K_{CD}}{\tau_{CD}} \propto \left(L_g^2\right) \tag{34}$$

The inertia divided by torque rule is represented in Fig. 7, where we can appreciate that it only provides a good trend prediction for the PGT. For stiffness divided by torque, the prediction of equations (28), (31), and (34) did not lead to a good match for none of the gearboxes. Fig. 8 represents an empirical scaling law indicating that stiffness tends to follow the same trend as acceleration torque.

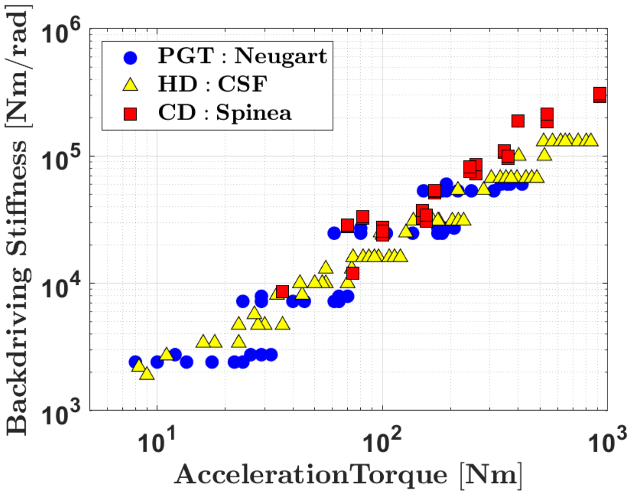

Figure 8. Correlation between backdriving stiffness and acceleration (maximum repeatable) torque capacity for Planetary Gearboxes (Neugart, Alpha series), Harmonic Drive (CSF, CSG, SHF, SHG, HFUS series), and Cycloid Drive (Spinea, G, GH, T, E, H, M series) gearboxes.

3.4.2 Motor torque scaling

Haddadin et al. validated experimentally [17] the following scaling law for the stall torque $\tau_{m,max}$ of an electric motor:

$$\tau_{m,max} \propto \left(L_m \cdot d_m^{5/2}\right) \tag{35}$$

This allows us to relate torque capacity and backdriving inertia in the following scaling law, which could not be validated empirically, see Fig.9:

$$\frac{\tau_{m.max}}{J_m} \propto \left(d_m^{-3/2}\right) \tag{36}$$

4 Influence of the operating cycle

The operating conditions have a substantial influence on an actuator's backdrivability, first and foremost, through the direct impact of torque, position, speed, and acceleration on the motion equation (1), but also through the effect of these elements on gearbox and motor losses.

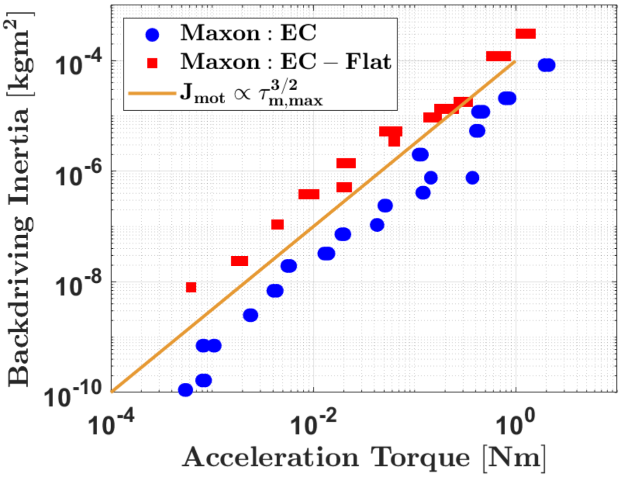

Figure 9. Correlation between backdriving inertia and acceleration (maximum repeatable) torque capacity (estimated as 2.5 times the catalogue's nominal torque) for Maxon EC and EC-Flat electric motors. The correlation seems to follow an empirical scaling rule given by $J_m \,\alpha\, \tau_{m.max}^{1.5}$ that does not directly correspond to equation (36). Also note that, for a given torque, the flat motors always have considerably larger inertia. This on the other side correlates well with equation (35): the larger diameters of a flat motor configuration have a stronger impact on inertia than on torque.

Accordingly, to assess the backdrivability of an actuator for a certain application, we must identify the operating conditions at which backdriving will occur, differentiating between breakaway backdriving (is the backdriving torque sufficient at the operating points where the backdriving condition is initiated?) and regenerative backdriving (is the backdriving efficiency sufficient at regenerative operating conditions to enable regeneration?).

Practically, this can be done by first identifying the operating cycle points where the actuator changes from forward-driving to backdriving operation and vice versa. This can be made either by reversing speed (need to overcome static friction) or by reversing torque (need to overcome backlash only). A transition from forward-driving to backdriving characterizes a point in the operating cycle where we must verify if the backdriving torque is enough to overcome the actuator's backdriving friction and if the actuator's inertia is low enough to enable the remaining useful torque to induce the required backdriving acceleration. Failing to overcome friction and/or induce the backdriving acceleration at the switch point indicates that the actuator is not suitable for the backdriving needs of the system.

Once this first step is cleared, we can try use the actuator's backdriving parameters from section 2 to assess the regenerating capacity during the backdriving period that follows this transition point.

4.1 Example of a Knee Prosthesis

In [21], Tucker and Fite analyze how mechanical damping affects regeneration for a powered transfemoral prosthesis. Verstraten et al. present also a more recent study in [22] this time for an ankle prosthesis, in which the effect of backdrivability and regeneration are also incorporated. Here, we include a basic yet illustrative analysis of how regeneration is affected by actuator's backdrivability for a knee prosthesis. A knee prosthesis is particularly interesting because, during normal walking, the human knee sees frequent bidirectional power flow: to enable walking, the knee injects power into the leg (positive power), but it must also absorb mechanical power (negative power), as we can see in Fig.10. A prosthesis capable of mimicking this behavior must include a backdrivable actuator, capable of absorbing energy – ideally in an efficient manner – when the mechanical power is negative.

As an example, we select for the actuator of our knee prosthesis a Harmonic Drive SHF-17-120 with a gear ratio of 120:1 and an acceleration torque of 54Nm, larger than the max. absolute load torque of the knee (46Nm, see Fig.10). We combine this gearbox with a 90Watt Maxon EC45 Flat motor with a nominal torque of 0.167Nm, which will need to produce an output torque 3x larger than its nominal torque (0.5Nm) to produce the 46Nm required at the output of the HD gearbox, which has an efficiency of 75%. The main backdriving relevant parameters of this combination can be extracted from their respective catalogs and are given in Table I.

Table I. Key SHF-17-120 HD gearbox and 90Watt Maxon EC45-flat motor parameters extracted from their respective catalogs, combined to build an actuator for the knee prosthesis. The motor's backdriving stiffness is calculated from equation (7), based on the dimensions of its output shaft. The dynamic viscous coefficient of the gearbox is calculated from the catalog's efficiency graphs at different speeds. The motor dynamic viscous coefficient calculated using equation (23).

Actuator's Parameters	80Watt EC45 Flat motor	SHF-17-120 HD Gearbox
Inertia (kgcm2)	0.135 (rotor)	0.193
Min. Backdriving Stiffness (Nm/rad)	(70000)	10000
Max. Backdriving Torque (Nm)	?	34
Peak Efficiency	85%	75%
Terminal Resistance (Ω)	0.447	-
Torque Constant (Nm/A)	0.0295	-
No load Speed (rad/s)	600	-
No load Current (A)	0.281	-
Dynamic Viscous Losses coefficient	$D_{mD} \approx 0.00014$	$D_{gD} \approx 0.05$

Using equations (10), (11) and (14), and assuming dynamic Coulomb friction to be around 50% of the starting torque for the gearbox, this leads to the following losses:

$$\tau_{R,m} \approx \frac{0.447}{(120 \cdot 0.75 \cdot 0.0295)^2} \cdot \frac{\tau_{bck}^2}{\eta'_O \cdot \dot{\theta}_O} = 0.0475 \cdot \frac{\tau_{bck}^2}{\eta'_O \cdot \dot{\theta}_O} \quad (37)$$

$$\tau_{D,m} = 120 \cdot D_{mS} \cdot e^{-120 \cdot \beta_m \cdot \dot{\theta}_O} + 2.02 \cdot \dot{\theta}_O \quad (38)$$

$$\tau_{C0,g} \approx \frac{34}{2} = 17Nm \quad (39)$$

$$\tau_{L,g} \approx 0.2 \cdot \tau_{bck} + 17 + D_{gs} \cdot e^{-\beta_g \cdot \dot{\theta}_O} + 0.05 \cdot \dot{\theta}_O \quad (40)$$

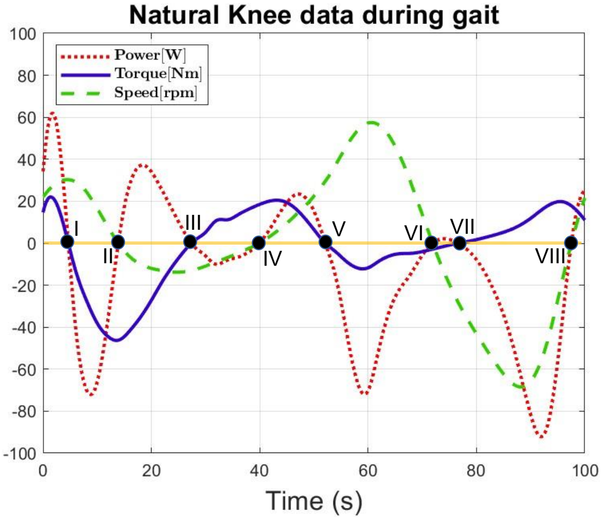

Fig. 10. Mechanical power (Watt), torque (Nm), and speed (rpm) vs. time of a human knee during walking at normal speed for a 75kg person, data from [20]. For a knee prosthesis trying to mimic this reference cycle, negative power indicates that the actuator should be backdriven and have the ability to regenerate between I to II, III to IV, V to VI, and VII to VIII.

Using equations (6) and (15), the backdriving inertias and stiffnesses of the gearbox (g) and motor (m) are:

$$J_{bck,g} \approx 120^2 \cdot 0.193 = 2.78kgm^2 \quad (41)$$

$$J_{bck,m} \approx 120^2 \cdot 0.135 = 1.94kgm^2 \quad (42)$$

$$K_{bck,g} \approx 10000Nm/rad \quad (43)$$

$$K_{bck,g} \approx 70000Nm/rad \quad (44)$$

We can see that we do not have enough data to identify the terms $D_{gs} \cdot e^{-\beta_g \cdot \dot{\theta}_O}, \tau_{C0,g}, 120 \cdot D_{ms} \cdot e^{-120 \cdot \beta_m \cdot \dot{\theta}_O}$. If we assume that these can be neglected for an initial evaluation, we can now write equation (1) as:

$$\tau_{bck}\left(0.8 - \frac{0.0475 \cdot \tau_{bck}}{\eta'_O \cdot \dot{\theta}_O}\right) - 17 - 2.07 \cdot \dot{\theta}_O == 4.7 \cdot \ddot{\theta}_O + 8750 \cdot \theta_O \quad (45)$$

On Fig.10, we can identify the transition points from positive to negative power, marked as I, III, V, and VII. The transition points from negative to positive power are II, IV, VI, and VIII. This defines four periods of negative power – and thus actuator backdriving: I to II, III to IV, V to VI, and VII to VIII. Note that the transition points I, III, V, and VII where these negative power periods are initiated correspond all to zero-torque, thus without static friction (non-zero speed).

- Negative power section I-II:

Breakaway: according to the data from [20], point I corresponds to instant 4.6 sec. and to a backdriving torque of 0Nm. Of the up to 34Nm of torque required to initiate the backdriving movement, around half of it (17Nm) is required to maintain movement as the torque sign changes. This means that the available backdriving torque is initially insufficient to backdrive the gearbox and thus, if we would stop the motor supply of torque, the actuator would be blocked. To enable the actuator to follow the required speed trajectory, the motor must actually continue to deliver positive power.

Regeneration: once the backdriving torque exceeds the 17Nm (at instant 6.5 sec.) required to backdrive the gearbox, backdriving is enabled and the motor starts to have the ability to regenerate energy. At instant 13.9 sec., the angular speed becomes zero and the motor must again deliver power. In Fig.11 we can see that, once we consider the losses and the torque required to accelerate, the regeneration capability is substantially limited.

- Negative power sections III-IV, V-VI, VII-VIII:

During the next three sections with negative power, the torque is not enough to overcome friction (see Fig. 11) and the system is non-backdrivable, making regeneration not viable: although the system is trying to inject mechanical power into the actuator, the non-backdrivable condition forces the motor to provide positive power to enable the knee to follow the target trajectory.

Globally, Fig. 11 shows that the electrical power required to enable the knee prostheses to follow the torque-speed trajectory of a human knee during natural gait is an order of magnitude larger than the mechanical power required by the human knee itself. This is the consequence of the low backdriving performance of the selected actuator, combined with the relatively high starting torque of the gearbox.

In terms of backdrivability, friction is clearly the main responsible of the poor backdriving performance of this actuator. The high backdriving breakaway torque of the HD gearbox strongly makes that only during about 2/3 of the time of the I to II period is backdriving operation possible. Additionally, once the movement is initiated, a large amount of the backdriving energy is lost in mechanical and electrical losses in gearbox and motor.

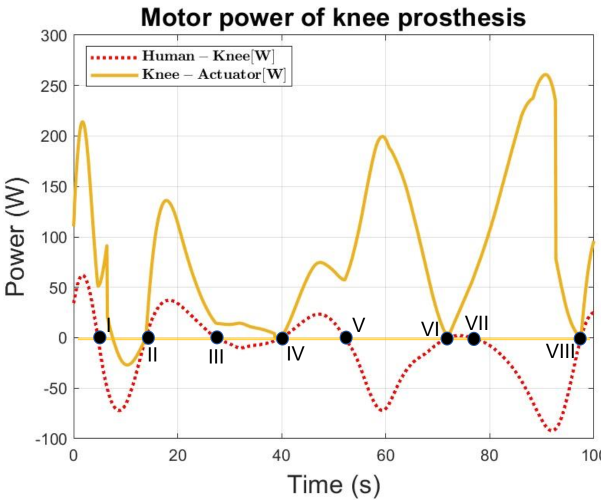

Fig. 11. Comparison of the power vs. time of a human knee during walking at normal speed for a 75kg person, with the electrical power required by a knee actuator composed by an SHF-17-120 HD gearbox and a 90Watt Maxon EC45-flat motor. The frequent backdriving operation (negative power) of the human knee and the low backdrivability performance of the actuator strongly limit the regeneration potential, which his only possible in the time between 6.5 and 13.9 sec. Additionally, the

low torques and relatively high speeds, combined with the high starting and backdriving torques of the HD gearbox, require over-dimensioning the actuator's motor to match a max. (positive) power demand four times larger than the human knee.

5 Conclusions

Actuator backdriving is a frequent condition in human (and more general in animal) movement that derives from the need to enable bidirectional power flow in our interactions with the environment. This need is naturally extended to human-centered robotic devices that, in order to perform their activities, must themselves interact directly with humans and their environments.

Traditionally, high speed-reduction ratio gearboxes have been associated with actuators with low backdrivability due to the substantial impact of high-speed ratios on reflected inertia. Our analysis invalidates this hypothesis and provides an alternative model of backdrivability that reflects the influence of a large number of factors and demonstrates the need for a much broader perspective to reach a reliable assessment. Instead of considering only inertia and the effect of the squared speed-reduction ratio, our model complemented with some scaling laws show the relevance of how speed-reduction ratio affects motor inertia, as larger motors are needed to compensate for lower speed-ratios. This is particularly relevant as dimensional changes strongly impact inertia and efficiency affects how this inertia is reflected to the gearbox output. Stiffness and the losses of gearbox and motor can also have a substantial contribution, particularly in combination with the specific operating conditions. In section 4 we demonstrate how limited actuator backdrivability is largely responsible for the substantially larger power consumption of an actuated knee prosthesis, compared to a human knee.

Some parameters required to assess an actuator's backdrivability accurately are not available from the manufacturer's datasheets. Nevertheless, our model provides the possibility to combine available data with basic scaling laws to assess the backdriving performance of an actuator and guide the selection of a suitable actuator considering its backdriving performance. Two significant limitations to this approach are the motor's mechanical losses and the backdriving stiffness, for which we provide some practical assumptions to compensate for the absence of commercial data and relevant research studies.

A relevant limitation of this study lies in the non-consideration of the motor driver, that can have substantial influence on losses during regenerative backdriving. Also, the relevance of magnetic stiffness between the motor's rotor and stator could not be established, to validate the assumption of the higher relevance of the rotor's mechanical stiffness.

Derived research directions include (i) the study of the stiffness of electrical motors, to validate our hypothesis in section 3.3.2 and search for generic and accurate scaling laws, (ii) the characterization of the mechanical losses of commercially available electric motors, including the recently proposed high-torque motors, (iii) the search empirical scaling laws to help us predict trends of inertia in HDs and understand how gearbox inertia and stiffness relate to torque, and (iv) to extend the list of manufacturers and models and broaden our understanding of the validity of the proposed scaling laws.

References

1. Ishida, T., & Takanishi, A., IEEE Int. Conf. Robotics, Automation and Mechatronics, pp. 1-6 (2006)
2. Nef, T., & Lum, P., *Medical & biological engineering & computing*, **47**(4), 441-447 (2009)
3. Zinn, M., Khatib, O., Roth, B., & Salisbury, J. K. IEEE Robotics & Autom. Mag., **11**(2), 12-21. (2004)
4. Kaminaga, H., Ono, J., Nakashima, Y., & Nakamura, Y., IEEE Int. Conf. Robotics & Autom., pp. 1577-1582, (2009)
5. Sensinger, J. W., & Weir, R. F., Int. Conf. Rehabilitation Robotics ICORR, pp. 390-393, (2005)
6. Seok, S., Wang, A., Otten, D., & Kim, S., IEEE Int. Conf. Intel. Robots & Systems, 1970-1975, (2012)
7. Ducastel, V., Langlois, K., Rossini, M., Grosu, V., Vanderborght, B., Lefeber, D., & Geeroms, J., *Actuators*, **10-11**, p. 289, 292, (2021)
8. Segil, J. (Ed.), *Handbook of Biomechatronics*. Academic Press, (2018)
9. Garcia, P. L., Crispel, S., Varadharajan, A., Saerens, E., Verstraten, T., Vanderborght, B., & Lefeber, D. IEEE Int. Conf. Robotics & Autom ICRA (2022)
10. Niemann, G., Winter, H., Höhn, B. R., & Stahl, K., *Maschinenelemente*, Springer-Verlag, (2019)
11. Talbot, D. C., Kahraman, A., & Singh, A., ASME J. Mech. Des., **134** (2): 021003, (2012)
12. Wang, A., & Kim, S., IEEE Int. Conf. Robotics & Automation, ICRA, pp. 1055-1062, (2015)
13. Verstraten, T., *New actuation paradigms with high efficiency for variable load at varying speed*, doctoral dissertation, Vrije Universiteit Brussel, (2018)
14. Verstraten, T., Mathijssen, G., Furnemont, R., Vanderborght, B., & Lefeber, D., *Mechatronics*, **30**, 198-213, (2015)
15. S. A. Nasar and I. Boldea, *Electric Machines: Steady-State Operation*. Taylor & Francis, (1990)
16. Saerens, E., Crispel, S., Garcia, P. L., Verstraten, T., Ducastel, V., Vanderborght, B., & Lefeber, D., *Mech. & Machine Theory*, **140**, 601-621, (2019)
17. Wensing, P. M., Wang, A., Seok, S., Otten, D., Lang, J., & Kim, S., IEEE Trans. on Robotics, **33(3)**, 509-522, (2017)
18. Haddadin, S., Mansfeld, N., & Albu-Schäffer, A., IEEE/RSJ Int. Conf. Intel. Robots & Systems, 5097-5104, (2012)
19. Verstraten, T., Mathijssen, G., Furnemont, R., Vanderborght, B., Lefeber, D., *Mechatronics*, 198-213 (2015)
20. Winter, D. A., John Wiley & Sons, *Biomechanics and motor control of human movement*, (2009)

21. Tucker, M.R. & Fite, K.B., IEEE Int. Conf. Advanced Intelligent Mechatronics, pp.13-18, (2010)
22. Verstraten, T., Geeroms, J., Mathijssen, G., Convens, B., Vanderborght, B., & Lefeber, D., *Mech. & Machine Theory*, **116**, 419-432, (2017)